water

MDPI

Article

Non-Intrusive Measurements of Wave-Induced Flow over Dikes by Means of a Combined Ultrasound Doppler Velocimetry and Videography

Maria Gabriella Gaeta *, Massimo Guerrero, Sara Mizar Formentin, Giuseppina Palma and Barbara Zanuttigh

Department of Civil, Environmental, Chemical and Materials Engineering, University of Bologna, viale del Risorgimento 2, 40136 Bologna, Italy; massimo.guerrero@unibo.it (M.G.); saramizar.formentin2@unibo.it (S.M.F.); giuseppina.palma2@unibo.it (G.P.); barbara.zanuttigh@unibo.it (B.Z.)

* Correspondence: g.gaeta@unibo.it

Received: 29 September 2020; Accepted: 28 October 2020; Published: 30 October 2020

Abstract: The performance of non-intrusive instruments, such as acoustic profilers and cameras, to describe the wave-induced flow processes over maritime dike crest was investigated in experiments carried out at the University of Bologna. Direct and derived measurements from the acoustic probes deployed along the structure crest were discussed in relation to the observed backscatter rates. Image processing was implemented by means of clustering algorithm, in order to detect the free surface during overtopping events and characterize wave front propagation over the dike crest. UVP data were processed to indirectly derive flow depths and overtopping rates and compare them with the direct measurements in order to assess the measurement reliability and discuss their limits. Individual overtopping volume distribution as obtained by UVP data were estimated and compared with well-consolidated formulations, showing a good agreement. Finally, suggestions for an appropriate use of non-intrusive instruments to characterize a shallow, transient and aerated flow were provided, such as the control of the artificial seeding density, the use of a bi-static UVP configuration and adjustments to light exposure.

Keywords: ultrasound Doppler velocimetry; image processing; overtopping discharge; wave-induced flow; non-intrusive instrumentation

1. Introduction

Wind-generated water waves, together with dam-break, impulsive waves and tsunamis, constitute fast-flowing, transient and turbulent processes with rapid level oscillations and largely aerated interactions with environment and structures. Therefore, measurements of wave-induced flow on dikes require appropriate design of the experimental set-up and adequate choice of the instruments [1,2] to be adopted, in order to (i) guarantee high standards of the acquired data (e.g., appropriate sampling frequency and spacing resolution, stability, accuracy, and instrumental integrity during tests), (ii) reduce their overall disturbance to the process being measured, and (iii) provide data to be easily (post-) processed with unique and unambiguous meanings.

The experimental characterization of the interactions between waves and dikes in terms of water depths, velocities, loads, and overtopping discharges remains a challenging issue due to the unsteady non-linear dynamics, like breaking, turbulence, and air entrainment [3,4], as well as over-washing processes, eventually alternating wet and dry conditions on the crest [5–8].

Instruments like wave gauges and micro-propellers are defined as intrusive [9] to experimentally characterize the flow over the dike crest during overtopping, and in particular for small-scale tests;

indeed, they generate unwanted wakes in a thin water layer (especially in the case of emerged rarely overtopped structures) and provide only point-wise measurements of the flow, such as water elevation and speed at a single location. These in turn limit the measuring range of depths and velocities, due to the minimal dimensions and their initial inertia of motion, resulting in ultra-shallow (less than 10 mm) and ultra-slow flow (less than 1 cm/s) not measured by conventional instrumentation [7].

To overcome these limitations, the development of laser, acoustic and optical/video analyses have already led to promising results also in the field of coastal engineering, such as to measure wave run-up processes on beaches (e.g., [10–12]).

Ultrasound Doppler Velocity Profiler (hereinafter UVP) allows for direct measurements of the flow velocities in liquids by exploiting the Doppler frequency shift between emitted and received signals. The use of UVP is well established in a variety of fluid mechanics and hydraulics applications, among others, including measurement of river flow [13,14] and the control of liquid metal flow for continuous casting as in [15]. UVP can also be installed inside the modelled structures through mounting holes, guaranteeing a good coupling between the transducer and the liquid by filling empty spaces with echography gel. These profilers were deployed in this way to measure, for instance, the flow impact triggering the motion of boulders during small-scale tests of tsunami-like waves in flume [16].

The advantage of their use mainly derives from the possibility of non-intrusive measuring of fluid velocity, also in harsh conditions and in shallow waters, and allowing for instantaneous velocity profiles and great adaptation to changing flow conditions and boundaries. In the field of coastal studies, previous relevant experiments by using acoustic probes in transient and aerated flows were carried out by [17,18], for dam break waves, and by [19], for submerged dikes, proving the effectiveness of such technique to characterize unsteady dynamics. However, the measurement of the water depths over the structure crest and the reconstruction of the related wave overtopping discharges have not been tested to date. At the same time, the development of advanced optics and laser systems and the implementation of image processing by means of high-performance computers [20] gave rise to experimental techniques to detect the free surface and estimate the flow velocity.

Some researchers (among the others, [21–23]) proposed alternative methods based on videography to reconstruct water elevation by side-wall camera, and the technique was also used to investigate sand bed evolution in nearshore zone [24,25] and the performance of floating bodies [26,27]. More complex optical approaches, like Particle Tracking Velocimetry (among the others, [28,29]), Particle Image Velocimetry (among the others, [30,31]), and Bubble Image Velocimetry (among the others, [32]) were shown to provide accurate results in the description of velocity field (i.e., streamlines, pathlines) and air entrainment during wave breaking and impacts [33,34], but only a few studies [35–37] examined wave overtopping process at dikes through image-based techniques.

This paper investigates the performance of non-intrusive instruments, such as UVP and camera. The aim is to provide practical suggestions for their usage limitations and setting when measuring the wave-induced flow over dike crest and reconstructing the mean and individual overtopping discharges.

The paper is organized as follows. Section 2 briefly describes the experiments performed in the wave flume of the Laboratory of Hydraulic Engineering at the University of Bologna (Italy) to investigate wave-induced overtopping process, including the instrumental apparatus used to characterize developing dynamics over the dike crests. The data processing together with assumptions and limits for the implemented analysis are reported in Sections 3 and 4, where flow analysis by UVP measurements and the free-surface detection through the image processing are illustrated in detail.

The performance of proposed methods to measure water depths and velocities over the dike crest as well as overtopping discharges are presented in Section 5, showing comparison with the well-consolidated formulae provided by the EurOtop manual [38]. Finally, concluding remarks regarding the most appropriate instrument setting are drawn in Section 6.

2. Description of the Laboratory Tests

New experiments on wave overtopping at dikes have been carried out at the University of Bologna in the wave flume depicted in Figure 1. This is 12 m long, 0.5 m wide and 1.0 m deep, and waves are generated by the vertical movement of a cuneiform-shaped piston-type wave-maker defined on the basis of mass conservation law [39,40] and described in detail by [41]. The generated irregular waves were characterized by values of significant wave height H_s in the range 0.04–0.06 m and peak wave periods T_p in the range 0.85–1.51 s, with corresponding values of the wave steepness $s_{m-1,0} = H_s/L_{m-1,0} \approx 0.03$–$0.04$. The duration of each test was equal to 10 min, in order to reproduce between 500 and 700 individual waves in the flume.

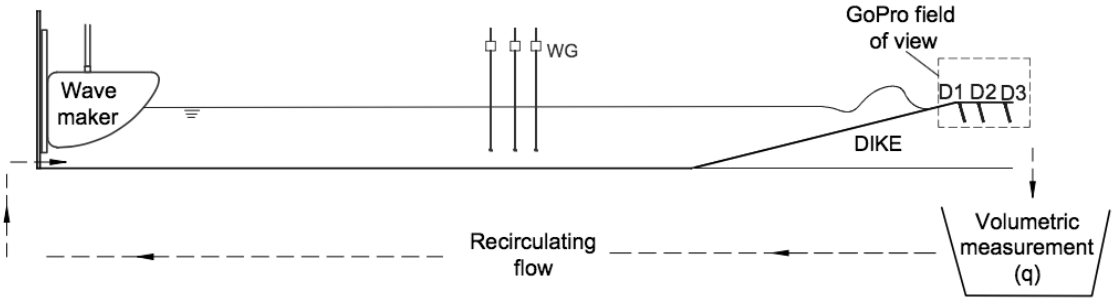

Figure 1. Sketch of the wave flume (Not to Scale) and layout of the used instruments: three WGs at the middle of the channel, three UVP probes along the dike crest (namely D1, D2 and D3), GoPro recording window, tank for q measurement (i.e., overtopping cumulated volume), and recirculation flow system.

The wave attacks were performed against four dikes, built in polymethyl methacrylate (PMMA), whose cross-sections differ for the crest widths, G_c = 0.15 and 0.3 m, and/or the seaward slope, $\cot(\alpha_{off})$ = 2 and 4. Therefore, four dike configurations were realized with height equal of 0.35 m and were positioned in the right-hand side of the channel, at a distance of around 11 m from the wave-maker, as indicated in Figure 1. Each dike configuration was tested at three crest-freeboard conditions, R_c/H_s = 0, +0.5 and +1, obtained by varying the water depth wd in the channel from 0.29 to 0.35 m. For each freeboard, several tests were performed, by varying the values of H_s and T_p, resulting into a total of 54 tests. The summary of the tested configurations is given in Table 1.

Table 1. Summary of the target conditions of the experiments of wave overtopping at dikes.

R_c/H_s	0	+0.5	+1
$s_{m-1,0}$ (%)	3; 4	3; 4	3; 4
$H_{s,m-1,0}$ (m)	0.04; 0.05; 0.06	0.04; 0.05; 0.06	0.05; 0.06
wd (m)	0.35	0.32; 0.325	0.29; 0.30
cot (α_{off})	2; 4	2; 4	2; 4
G_c (m)	0.15; 0.30	0.15; 0.30	0.15; 0.30

The wave-flume was equipped with the following instruments:

- three wave gauges (WG), placed at approximately 1.5 times the maximum $L_{m-1,0}$ from the wave-maker (≈ 5 m) to record the free-surface elevation with a sampling frequency of 100 Hz and to separate the incident and reflected waves, according to [42];
- three UVP probes, which were installed along the structure crest and were used to record the time series of the vertical profiles of the horizontal flow velocities (u) and track the free surface elevation or water depth (h). These ultrasound probes were located in proximity of the off-shore edge (D1), in the middle (D2) and close to the in-shore edge (D3) of the dike crest;
- a 30 Hz GoPro camera employed to film in Full HD resolution the wave run-up, flow over the crest and overtopping process; the GoPro was placed at exactly perpendicular positions to the side window of the wave flume where the dike was located (Figure 1);

- a tank for the storage and measurement of the wave overtopping volumes, placed at the end of the wave flume and below the channel (Figure 1), to calculate the cumulated overtopping volume at the end of each test;
- a recirculation system, connected to the channel in order to preserve the water depth throughout the experimental duration.

The analysis of the results in terms of reflection coefficients and overtopping rates was presented in [41], where a good agreement of the experimental data with most widely used formulae was shown together with proposed guidelines to update the state-of-the-art formulae for a more cautious estimation of the water depths and velocities of propagation of the flow in the landward area.

3. UVP Data Analysis and Processing

3.1. Overview of Basic Concepts

The UVP is a monostatic sonar emitting and receiving short bursts composed by acoustic pulses to measure profiles of flow velocity within liquids. This device was originally developed to provide spatio–temporal information of a fluid flow [43] by exploiting the Doppler effect: When enough scattering particles seed the fluid flow, the emitted pulses are scattered back to UVP receiver, which experiences a Doppler shift, f_d giving the measured radial velocity

$$v_r = \frac{c \cdot f_d}{2 f_0} \tag{1}$$

where f_0 is the emitted frequency, and c is the sound speed in water.

The measurement of f_d is commonly assessed by using an autocorrelation function at a lag equal to pulse repetition period T_{prf}, namely the pulse-pair method [44]. This uses consecutive pulses in pairs, required in a number of pairs necessary to increase the statistic stability of the final results [45]. This technique limits T_{prf} to the observation time among consecutive pairs of pulses. As a consequence, the maximum distance of measured velocity (i.e., the ranging distance, r) should be lower or equal than two times the traveling distance of sound pulses:

$$2r \leq c \cdot T_{prf} \tag{2}$$

In analogy with the Nyquist–Shannon theorem for continuous signal sampling into discrete time series, the Doppler shift must be smaller than the Nyquist frequency, limiting the maximal measured value of f_d and flow velocity for a given pulse repetition frequency ($f_{prf} = T_{prf}^{-1}$), as described in Equation (3):

$$f_d \leq \frac{f_{prf}}{2} \tag{3}$$

In the present experiments, probe frequency f_0 was set to 4 MHz in order to have the value of f_{prf} equal to 11,904 Hz and a profile resolution of 1.01 mm. Using a Doppler angle of 75° and assuming the overtopping flow mostly aligned with the dike crest (i.e., horizontal), Equations (1)–(3) yielded around 70 mm as maximum distance from the probe and 4.2 m/s for maximum velocity, respectively.

3.2. Scattering Process and UVP Limitations

Ultrasound scattering, acoustic beam geometry and sound reflection at water–air interface play a relevant role in determining the UVP performance. The sound reflected and refracted by scattering particles is usually referred to as volume scattering [46]. The overall sound reflected back to UVPs from water–air interface, hereinafter referred to as surface scattering, is usually stronger than the volume backscattering and was eventually processed to detect free surface position. In fact, the profiled echo intensity level, EL, was converted into the backscatter, BS, by accounting for the spherical spreading

r^2 of the echo and by neglecting the other sources of sound dissipation (e.g., forward scattering, attenuation due to water viscosity):

$$BS = EL \cdot r^2 \quad (4)$$

The derived BS at each cell (i.e., by applying the actual ranging distance r of each gate in Equation (4)) embeds the volume and the surface scatterings. A shortcoming is revealed in cases of scarce seeding, and the surface scattering overwhelmed the volume scattering and saturated the UVPs during the receiving phase, as also experienced by [47]. Subsequently, the Doppler effect cannot be easily detected, especially close to water surface where the maximum surface scattering and velocities are usually expected to occur.

This UVP shortcoming is further exacerbated by side lobe interference. In fact, a finite circular piston focuses the acoustic power into a conic beam with side lobes, which radially protrude [48]. The half beam width φ, i.e., half of the angle at cone vertices containing most of the acoustic energy, and the used probes diameter d were equal to 1.22° and 4 mm, respectively (Figure 2a).

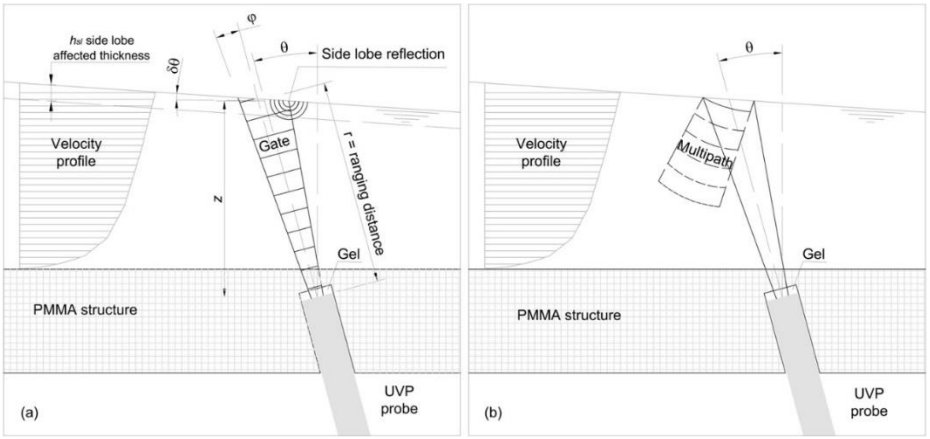

Figure 2. (**a**) Outline of UVP probe deploy at the dike crest with the acoustic beam geometry, the range gating and side lobe reflection. φ is the half beam width, z is the probe tip to water surface vertical distance, and θ and $\delta\theta$ indicate the beam angle with respect to vertical and the water surface slope, respectively. (**b**) Outline of the multipath following the reflection at the free surface.

As the UVP probe axis was not installed orthogonally oriented to the crest plane, the acoustic beam was initially reflected at the side lobe much closer to the vertical (i.e., orthogonal to water surface), and then followed the sound reflection at the central lobe axis. In fact, the downstream external beam arrived to the receiver before the central beam with axis of an angle $\theta = 15°$ (Figure 2a).

The surface reflection of this side lobe preceded and therefore masked the volume scattering from the central lobe, although it has higher energy. This resulted in a side lobe affected region where the flow velocities could not be measured. The extension of this region depended on the beam axis to water surface angle ($\theta + \delta\theta$ as outlined in Figure 2a), on the water depth, on the UVP deployment and on the beam geometry (i.e., θ, φ, d).

The side lobe affected thickness h_{sl} was assessed through trigonometric considerations (Figure 2a), as:

$$h_{sl} \cong \left(\frac{2z \cdot sin(\varphi)}{cos(\theta - \varphi)} + d \right) \cdot sin(\theta + \delta\theta) \quad (5)$$

The values of h_{sl} are reported in Table 2 for two combinations of the maximum vertical distance between the probe tip and the water surface and the water surface slope (i.e., z and $\delta\theta$ in Figure 2a). These values refer to the mean flow depth on the crest as they were observed for two different relative freeboards by means of image processing (described in Section 4) giving the possibility to achieve simultaneous water depths.

Table 2. Side lobe affected thickness h_{sl}-calculated as in Equation (5) with mean values of z and $\delta\theta$ (obtained from videography) for two combinations of R_c/H_s.

R_c/H_s	θ, φ, d	z(**mm**)	$\delta\theta(^\circ)$	h_{sl}(**mm**)
0	15°, 1.22°, 4 mm	30	5	1.8
+1		15	1	1.3

In the case of $R_c/H_s = 0$, the thickness of the side lobe affected region corresponded to about two times the profile resolution, i.e., equal to 2.02 mm. This was the worst condition and did not allow measuring the flow velocities at the water surface.

The water surface reflection also gave rise to a multipath effect (Figure 2b), corresponding to false positions of measured flow velocities, which were above the real free surface elevation. A portion of the acoustic energy bounced off at the water–air interface because of the strong impedance variation throughout the interface [46]. This gave rise to a reflected beam within the water depth, but with gates having longer path (i.e., with a delayed return to UVP) than the free surface depth. Hence, the corresponding velocity measurements appeared at longer distances in the UVP profile. This false positioning occurred for T_{prf} higher than two times the actual travelling time from the probe tip up to the free surface.

Due to the typical delay of the monostatic switching from emission to reception (i.e., ringing effect), a thin layer (namely, blanking distance) close to the probe tip could not be measured and, therefore, the probes were located within the PMMA structure of the dike crest, through blind holes filled by ultrasound-echography gel (Figure 2b), which enabled sound propagation throughout the structure.

3.3. Echo and Velocity Profiles Filtering

The filtering process of the UVP data is paramount to detect the correct values of depth and velocity from raw measured profiles of echo. There are two basic concepts of this analysis: (i) the gate position shows the maximum backscatter in correspondence to the free surface position, which is expected to be characterized by the peak value due to surface scattering, and (ii) the flow velocity originates from the Doppler effect, which requires a sufficient volume scattering from suspended particles.

The scatter density noticeably changed during overtopping (Figures 3a and 4a) because of transient variation in flow capacity, which is related to the square velocity [49]. Therefore, both the relevant volume backscatter and a certain variability in time of its values are expected for gates with valid flow velocities. On the contrary, low and steady values of the assessed backscatter indicated low concentration of suspended particles, which were not enough for accurate measurements. Furthermore, almost constant and low values of backscatter were measured close to blanking distance at false gates, located within the ultrasound gel and PMMA structure. This is visible in the measured echoes at gate distances shorter than 10 mm, as shown in Figures 3a and 4a.

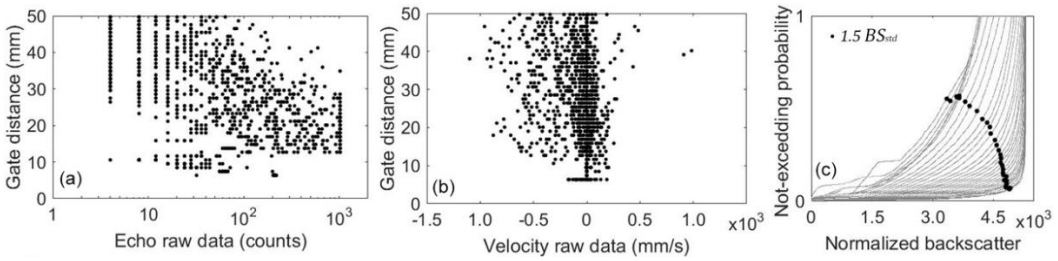

Figure 3. UVP analysis for a test with $R_c/H_s = 0$. Profiles of raw echo intensity levels (**a**) and velocities (**b**), negative values are for inshore direction; the probability distribution of normalized backscatter (BS_n) and corresponding threshold (BS_{std} indicated with dot marks) at each of the validated gates (**c**).

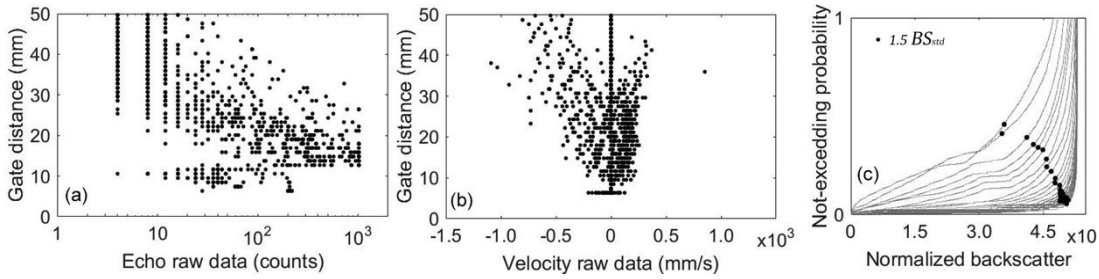

Figure 4. UVP analysis for a test with R_c/H_s = +1. Profiles of raw echo intensity levels (**a**) and velocities (**b**), negative values are for inshore direction; the probability distribution of normalized backscatter (BS_n) and corresponding threshold (BS_{std} indicated with dot marks) at each of the validated gates (**c**).

Therefore, the normalized maximum backscatter BS_{max} was assessed in Equation (6) as the maximum over the median values of the backscatter at each gate, giving low values at false gates and multipaths due to sound propagation into gel-PMMA and due to surface reflection, respectively.

$$BS_{max} = \frac{\max(BS)}{\text{median}(BS)} \tag{6}$$

Gates with BS_{max} lower than a specific threshold were rejected and the profile coherently trimmed to validated gates and re-aligned to the surface of dike crest. These thresholds were calibrated against the water depths and overtopping discharges as derived from videography and volumetric measurements, respectively. These thresholds changed from 5 to 25 and were inversely correlated with the dike freeboard, i.e., largest thresholds were found for zero freeboard. This indicated a limited performance of the UVPs in case of high overtopping rates, eventually inducing low volume scattering and prevalent surface scattering, which deteriorated the detection of the Doppler effect.

The normalized backscatter standard deviation was defined as:

$$BS_{max} = \frac{\max(BS)}{\text{median}(BS)} \tag{7}$$

where the standard deviation and the maximum backscatters were performed in time at each gate.

The assessed values BS_{std} were applied to filter time series of velocity (Figure 3b) at each of the previously validated gates. This filtering was performed on the basis of the normalized backscatter:

$$BS_n = \frac{BS}{\max(BS)} \tag{8}$$

Velocity values at sampling time and gate were rejected for low normalized backscatter, which indicated insufficient signal return from suspended particles. This also corresponded to low signal to noise ratio, and in these cases, the volume backscatter is too low for a reliable estimation of the Doppler velocity [50]. The minimum threshold for the normalized backscatter was calibrated versus observed flow depths and overtopping discharges, as described in Sections 4 and 5. This calibration resulted in rejecting the measurements with BS_n, not exceeding 1.5 times the corresponding BS_{std} at each cell. The probability of not exceeding a certain value of BS_n is reported in panels c of Figures 3 and 4, which also shows the corresponding thresholds (i.e., black dots at 1.5 times BS_{std}).

4. Image Processing: Implementation and Analysis

The main concept of image processing techniques, nowadays widely used in many hydraulics experiments, is the transformation of visual data into a digital RGB matrix [21,51] in order to derive features on fluid dynamics, depending on the image quality and the eventual seeding concentration [52,53]. In the present experiments, the installed GoPro camera recorded a video sequence of a field of view focused on the dike crest (as also shown in Figure 1) at a rate of

30 frames per second. The camera triggering with the wave generation was performed using the GoPro iOS application via Bluetooth. In order to improve the contrast among water and glass walls of the flume, black sheets covered the background of the recorded window, while strong lamps in a sort of dark room improved the image quality, giving an appropriate setting of the light exposure in the area of interest and reducing the background for the analysed image. Then, in post-processing, algorithms were implemented and applied to detect the free surface and characterize the flow depth during the wave overtopping. One of the most common methods to estimate the free surface elevation is the edge detection, firstly developed by [54], which consists of the identification of the image intensity gradient larger than fixed thresholds. It was successfully applied in hydraulics (among the others, [23,55,56]), but limited to cases characterized by smooth variation of surface slopes and low aerated fluids, where the discontinuities between the free surface and the remaining water body were evident and easy to be automatically captured by the algorithm.

Hence, this method was found to be insufficiently accurate to detect the free surface for the present experiments, due to the development of such highly turbulent and aerated flow as in case of wave-structure interaction [57]; therefore, the application of a clustering algorithm was preferred for these tests, where the possibility to estimate the air content could be also investigated and discussed.

The term clustering denotes a family of unsupervised automatic methods that can identify intrinsic groupings (i.e., clusters) of patterns in space, and defines classes in correspondence of these groups. Clustering has applications in numerous disciplines (e.g., pattern recognition, machine learning, computer vision) and was implemented for eco-hydraulics purposes [58,59]. The identification of the clusters follows two different criteria based on the minimization of (1) the sum of squares of pattern distances from centroids (i.e., barycentre) of the classes, and (2) intra-class distances in order to properly treat distribution with elongated ellipsoid shapes. Among the centroid-based algorithms, iterative methods, such as K-means, Fuzzy K-means and Expectation-Maximization (Gaussian Mixture) algorithms, are the most diffuse ones [60]. The latter was the one implemented in the Matlab toolbox called Pattern Recognition, originally developed by [61]. It was recently updated by [62] and adapted by the authors and used for the present experiments to analyse the acquired videos in order to characterize the flow over the crest and validate the reconstructed water depth data resulted by UVP.

For the camera settings, suggestions by reference [23] were followed in order to improve the image calibration and quality, e.g., using an array of exact grids made of clear acrylic sheets to check the lens distortion, mounting the camera in line with the structure crest, controlling its tilt angle to be vertically and horizontally aligned with the wave flume, and implementing the image processing algorithm only in the middle area of the image to reduce distortion and focus on the interested area.

The implemented algorithm (Figure 5) automatically allowed identifying the wave-induced flow thickness over the dike crest by means of the following steps:

(i) background removal, with the construction of a mask applied to the original video in order to remove the area of the frames to be neglected from the analysis (e.g., the zone below and behind the dike crest); each RGB image was then transformed into greyscale image (Figure 5a);

(ii) calibration process of estimating camera parameters by using the approach proposed by [63], where images of a planar checkerboard were used; limitations due to lens distortion, optical errors and 2D–3D projections were solved by removing the fish-eye effects and calibrating the camera by the [64] calibration method. The definition of a conversion factor (from pixel to mm) was performed by taking as input one sample image up to reach a maximum conversion error less than 1 pixel (around <0.3 mm in the present field of view). Finally, camera intrinsic (i.e., lens distortion coefficients) and extrinsic parameters were provided as calibration matrix for each test, to obtain the correspondence between the image and the space (real) points;

(iii) training, where classifiers were identified for some representative frames selected from each test video. Once chosen the number of labels M, depending on the image quality (e.g., light exposure, the flow patterns over the crest) and on the bubble entrainment (e.g., wave breaking), the image matrix was converted into a dataset of features, where pixels were classified into a number of

classes of membership M, giving the classifier matrix W. In the present analysis, the value of M ranged from 10 to 15 classes. This step was performed for each test day and camera calibration, since the identification of classifiers largely depended on environmental light conditions and glass cleaning, even if the glasses were carefully cleaned and the light conditions were maintained as unchanged as possible. Figure 6b shows as an example the class with the label 13 corresponding to the free surface;

(iv) image clustering, following the Expectation-Maximization (EM) partition technique based on Gaussian distribution mixtures of the dataset (Figure 5b). On the basis of the number M of classes defined in the training process and on the classifier matrix W, each frame of the video was clustered using the nearest mean classifier, which finally divided the image pixel (i.e., intensity) into M clusters. Iteration was performed in order to statistically stabilize the assigned labelling;

(v) pattern recognition, with the elaboration of suitable classifiers that identified the label corresponding to the free surface during the dynamics, e.g., wave run–up and overtopping flow over the dike crest (Figure 5c);

(vi) free surface detection, after filtering noise in the derived signals due to both air entrainment and water drops on the flume glass walls, which reduced the image quality and sharpness, and finally matrix conversion of pixel into meter by applying the calibration coefficients (Figure 5d).

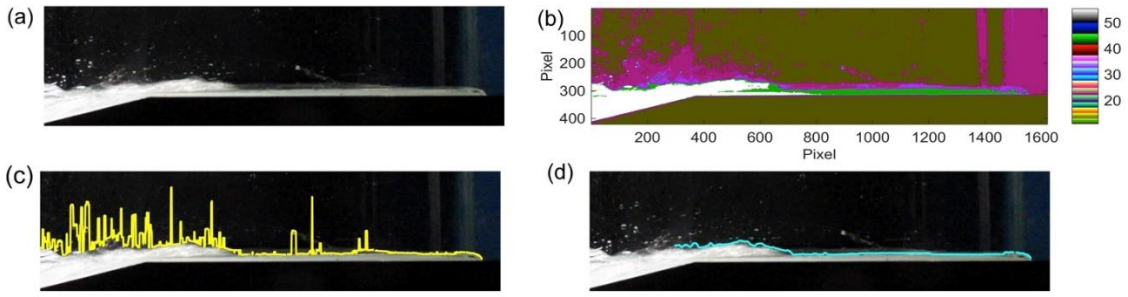

Figure 5. Example of test with R_c/H_s = +0.5. Steps of the implemented image processing to detect the free surface: original cropped frame (**a**), classification in clusters (**b**), and initial (**c**) and final detection of the free surface over the dike crest after the filtering process (**d**).

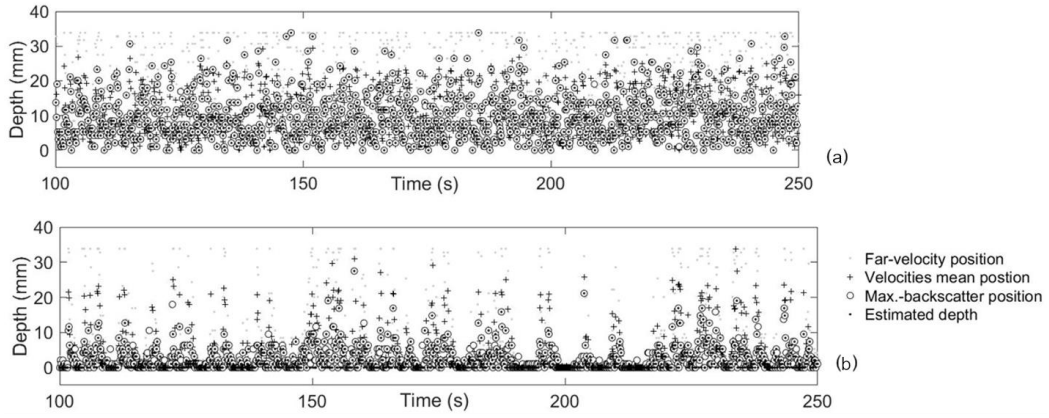

Figure 6. Estimated flow depth in time with positions of most far velocity, validated values of velocity (i.e., gates barycentre) and maximum backscatter: UVP analysis for test with R_c/H_s = 0 (**a**) and R_c/H_s = 1 (**b**).

5. Reliability of the Derived Non-Intrusive Measurements

The filtered backscatter and velocity profiles from UVP were analysed to evaluate the flow depths and the overtopping discharges at the dikes and compare to videography data and volumetric measurements in order to assess the reliability of the used non-intrusive instrumentations.

The values of h from UVP were generally detected at the gate with maximum backscatter, after an eventual profile re-alignment and filtering. When analysing the filtered profile of u, the farthest position of the gates where non-null velocity was measured (i.e., far-velocity position) and the barycentre of the validated values (i.e., velocities mean position) were derived. These outcomes can be compared to the estimated depths in Figure 6, which mostly corresponded to the maximum backscatter position with few exceptions in case of deteriorated profiles. In these cases, a clear peak in the backscatter profile was not detected or its height was typically much higher than the position of the remaining velocity data. For these noisy profiles (less than 10% of the validated), the velocities mean position was a more conservative estimate of the flow depth.

Overall, the implemented methodology efficiently performed among a broad range of conditions as it is demonstrated in Figure 6a for $R_c/H_s = 0$ and in Figure 6b, for $R_c/H_s = +1$. The gate corresponding to the far-velocity position frequently exceeded the assessed depth, clearly indicating velocity measuring at multipaths.

This case more frequently occurred when $R_c = 0$ (i.e., Figure 6a), which again was confirmed as the most challenging measurement condition in the case of prevailing surface scattering and side lobe interference. However, velocities at multipaths were used to eventually retrieve missing values close to the water surface due to the side-lobe effect. In fact, following the path of the reflected beam, some gates were available close to the water surface, which presented reliable values of velocity and were eventually characterized by a prevalent volume scattering (i.e., low value) farther than the peak along the profile.

5.1. Flow Depth over the Dike Crest

A comparison between the UVP data and the videography results was performed on a subset of 12 selected tests (i.e., H_s = 0.05 m, $s_{m-1,0}$ = 3%, R_c/H_s = 0, +0.5, +1; G_c = 0.15, 0.30 m; $cot(\alpha_{off})$ = 2, 4) in order to validate the methodology applied to the acoustic measurements as described in Section 3, where information on water depth was extracted by properly processing the echo and the velocity profiles.

Since the two instruments were not triggered and were set with different sampling frequencies, the spectra of the water depths derived from the two analyses were compared in Figure 7, where each panel reports data for different values of R_c/H_s, while keeping constant the wave condition (H_s = 0.05 m and $s_{m-1,0}$ = 3%) and the dike geometry (G_c = 0.30 m and $cot(\alpha_{off})$ = 4). For all three presented cases, the power spectrum density (PSD) values of water depth at D1 position over the crest from images and from UVPs was calculated by using Welch's overlapped segment averaging estimator [65], and their values were characterized by similar peak amplitude. In the case of $R_c/H_s = 0$ (panel a), the spectrum density was observed to be concentrated in a band equal to ± 0.5 the wave peak frequency, with a good correspondence in terms of peak frequency between the two data. In case of $R_c/H_s > 0$ (panels b and c) instead, quantities of energy related to the mean overtopping rates were also present at low frequencies due to rare overtopping events during the test, which is also in accordance to the observations by [66].

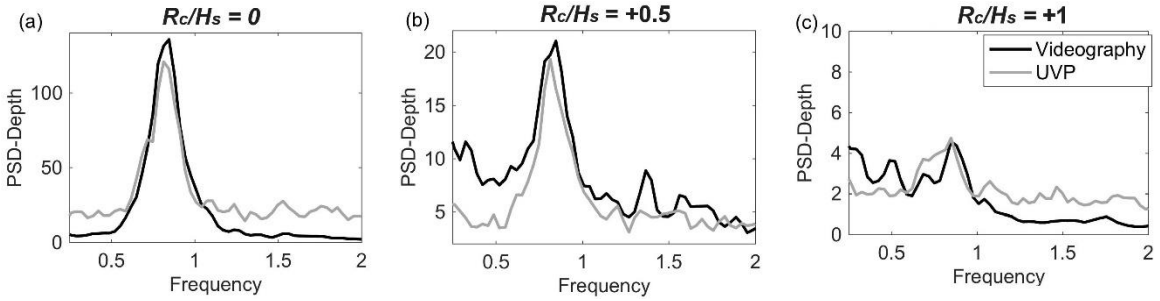

Figure 7. Comparison between water depth spectrum resulting from videography (black line) and UVP data (grey line) at D1: R_c/H_s = 0 (**a**), +0.5 (**b**) and +1 (**c**). Test with H_s = 0.05 m, $s_{m-1,0}$ = 3%, G_c = 0.30 m and $cot(\alpha_{off})$ = 4.

The overall reliability of the implemented image processing for the accurate detection of the free surface over the dike crest was verified at each test by overlapping the results with the corresponding frame, as it is also shown in Figure 5d.

The presented image processing was also applied to estimate the wave front propagation over the dike crest and reconstruct the maximum and mean water depth envelopes, as shown in [41].

5.2. Mean Wave Overtopping Discharge

Finally, the overtopping discharge as a function of the time, i.e., $q(t)$, was assessed by multiplying the flow depth derived from UVP (Figure 6a,b) with the corresponding depth-averaged negative velocities (where negative means wave-induced flow in-shore directed towards shoreline).

The time integral of wave-by-wave discharges obtained after the UVP filtering procedure provided values of q lower than the corresponding ones derived from cumulated volumetric measurements (Figure 8). The underestimation was slight (less than 10%) for low q in the case of emerged dikes (i.e., $R_c/H_s = +1$), but increased up to 50% for $R_c/H_s = 0$.

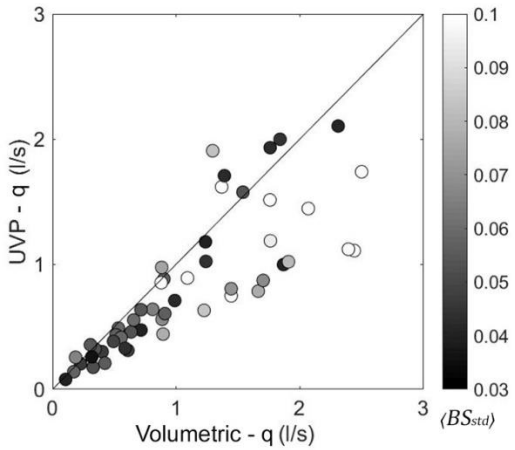

Figure 8. Comparison of mean overtopping discharge q as obtained by UVP and volumetric measurements. Color bar represents the normalized backscatter standard deviation $\langle BS_{std} \rangle$, which was averaged along the validated gates.

It is worth noting that low values of the normalized backscatter standard deviation $\langle BS_{std} \rangle$ (i.e., dark marks at the colour bar in Figure 8) resulted in better estimations of q. On the contrary, the UVP more significantly underestimated the assessed discharges in case of high $\langle BS_{std} \rangle$ (i.e., light marks). Indeed, the normalized backscatter standard deviation is a proxy of the UVP performance: Their high values give evidence of the probe saturation due to the strong sound reflection obtained from boundaries (i.e., the water-air interface), which disabled the volume scattering detection for Doppler velocimetry.

This phenomenon occurs in the case of (i) high value of maximum backscatter due to saturation and (ii) low variation of the backscatter from submerged gates into water. In this condition, the volume scattering at gates was most likely overwhelmed by the sound reflection at the water surface (i.e., surface scattering). This was especially the case of large depths where side lobe was more effective in masking the volume scattering, especially for large overtopping flow corresponding to low freeboards.

The time integral of wave-by-wave discharges obtained after the UVP filtering procedure (Section 3.3) was also compared with the well-consolidated formulae provided by the EurOtop

manual [38], providing the prediction of q in case of $R_c/H_s \geq 0$ and dry landward conditions following the expression:

$$q = min\left\{ \begin{array}{c} \frac{0.023}{\sqrt{\tan(\alpha_{off})}}\gamma_b \xi_{m-1,0} \cdot exp\left(-\left(2.7 \cdot \frac{R_c}{\xi_{m-1,0} H_s \gamma_b \gamma_v \gamma_f \gamma_\beta}\right)^{1.3}\right) \cdot \sqrt{gH_s^3} \\ 0.09 \cdot exp\left(-\left(1.5 \cdot \frac{R_c}{H_s \gamma_f \gamma_\beta}\right)^{1.3}\right) \cdot \sqrt{gH_s^3} \end{array} \right. \quad (9)$$

where γ_b, γ_v, γ_f, and γ_β are the influence factors for a berm, roughness elements on a slope, a crest wall, and oblique wave attacks; in this paper, all these factors are equal to 1, also according to [41].

The value of q obtained from UVP agrees with the formulae and the corresponding values from cumulated volumetric measurements. The latter values appear less scattered than the UVP estimates for the same relative freeboards (Figure 9). Furthermore, cumulated volumes result in larger values of q for null freeboard and Irribarren parameter ξ less than 1.8 (Figure 9b), i.e., in the case of breaking waves. Within this same range, the elaboration of the UVP data leads to underestimation with a maximum mean error equal to 40%.

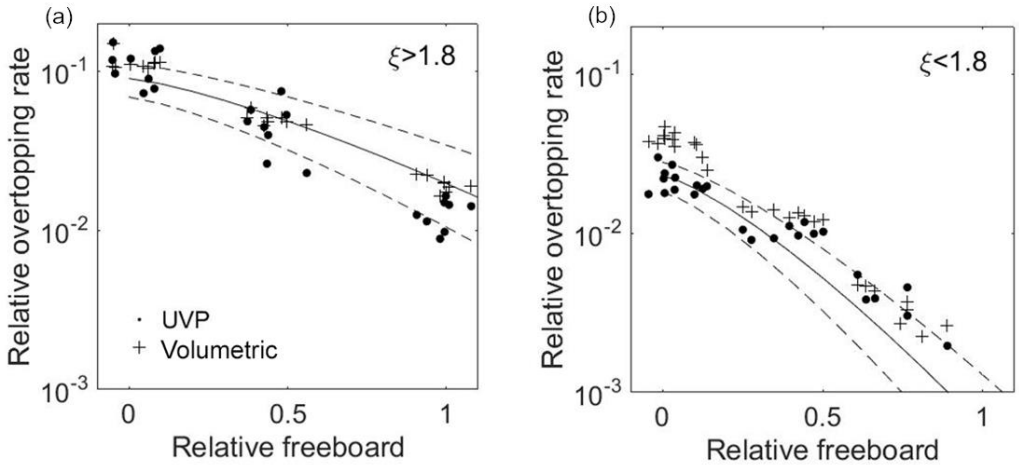

Figure 9. Relative overtopping discharge obtained from UVP (dot symbols) and from volumetric measurements (cross symbols), compared with the EurOtop formulae (5% under and upper exceedance limits in dotted lines). Panels (**a**) and (**b**) show tests with Irribarren factor ξ greater and less than 1.8, corresponding to the offshore slope equal to $cot(\alpha_{off})$ = 2 and 4, respectively.

5.3. Estimation of the Individual Wave Overtopping Volume Distribution

The first analyses on the individual wave overtopping volumes V at coastal structures were performed by [67,68] and later applied to traditional [69,70] and innovative sections [71], showing that the overtopping volumes essentially follow a Weibull distribution, characterized by scale and shape factors, namely a and b, respectively.

On the parameterization of b, [69,70] proposed a formulation depending on the relative crest freeboard in the case of low-crested steep slopes and over-washed dikes respectively, and [72] developed a new formulation for b as a function of the overtopping rate q for both permeable and impermeable structures and for any crest level. This formulation was also the one adopted by [38].

For a selection of the performed tests, where the UVP results were demonstrated to be accurate in comparison with the measured mean overtopping rates (i.e., the white and light grey circles in Figure 8 were excluded, as they do correspond to errors greater than 20%), the distribution of individual wave overtopping volumes was studied. For each test, the obtained values of V were treated as stochastic

variables and associated with an exceedance probability distribution that can be well represented by the two-parameters Weibull distribution [38], originally found by [68], as:

$$P(V_i \geq \overline{V}) = exp\left(-\left(\frac{V}{a}\right)^b\right) \quad (10)$$

where $P\left(V_i \geq \overline{V}\right)$ is the probability that the i-th individual volume V_i is greater than the specified volume $\overline{V}$.

Figure 10a shows the upper 20% exceedance probability distribution of V for a sample test with R_c/H_s = +1 and $cot(\alpha_{off})$ = 2. In the figure, the V-values are normalized with the mean volume of the distribution $\overline{V}$. The angular coefficient of the Weibull fitting line, reported in the panels together with the coefficient of determination R^2, is the b-factor. Overall, the data show a linear trend.

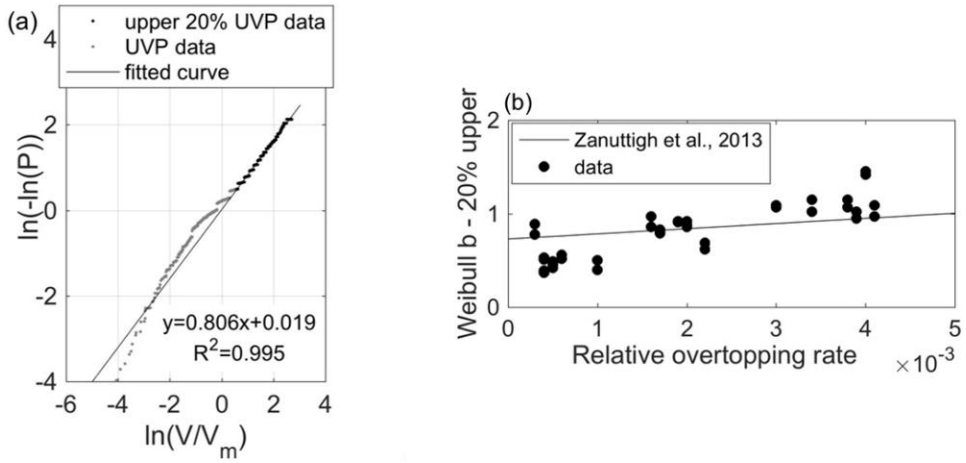

Figure 10. (**a**) Twenty percent exceedance probability distribution of V for an example of test with R_c/H_s = +1 and $cot(\alpha_{off})$ = 2. (**b**) Comparison between Weibull b-values derived from [72] and threshold probability distributions of individual volumes as derived from UVP dataset of all the performed tests.

Since the parameterization of the a-values is nowadays consolidated by the scientific community [38], the resulting b-values obtained from UVP data were compared (Figure 10b) with the formula presented by [72]:

$$b = 0.73 + 55 \cdot \left(\frac{q}{gH_s T_{m-1,0}}\right) \quad (11)$$

In the literature, there is no specific criterion to select the portion of the distribution of the overtopping volumes to fit the Weibull's b parameter [73,74]. Some authors suggest to fit b on the whole V-distribution, while other studies [70,75–77] adopt a certain percentage of the upper tail of the distribution (50%, 30%, 20%, and 10%) to get an estimate of b based on the "extreme" volumes only. Based on the analyses performed by [76], in this work the b-values were estimated from the upper 20% values of V-distribution. This choice yields results that are in good agreement with Equation (11) with maximum error of around 40% for few tests (see Figure 10b).

6. Conclusions and Suggestions

Small-scale experiments on wave overtopping over smooth dikes were carried out in the flume of the Laboratory of Hydraulic Engineering at the University of Bologna. Different irregular wave attacks and structure configurations were tested by varying the dike slope, the crest width and freeboard.

The overtopping of irregular waves at dike crest with null or positive freeboard is a transient process, leading to challenging conditions for measurements, since shallow and highly turbulent waters with aerated surfaces, including alternating dry and wet conditions, require instrumentations

with specific settings and low disturbance to flow propagation. For this purpose, three UVP probes, deployed along the structure crest, and a GoPro camera with a field of view focusing the dike, were adopted to measure the dynamics during wave overtopping, in addition to a volumetric tank to obtain the mean overtopping discharge values.

After filtering backscatter and velocity profiles on the basis of assessed thresholds on the normalized backscatter standard deviation and maximum values, the flow depths from UVP were indirectly derived and the mean overtopping discharge and the instantaneous overtopping volumes were assessed for each analysed test.

Image processing was implemented by means of a clustering algorithm for the detection of the free surface over the crest. After the image calibration and training to produce a classifier's matrix, the development of pattern recognition allowed obtaining water depths on the dike crest.

The derived water depths from UVP and images were analysed in terms of spectrum densities, while the mean overtopping discharges were compared with the volumetric measurements and with predictions by [38].

The simultaneous measuring of water depths and velocity profiles from UVP data allowed reconstructing the temporal evolution of the individual wave overtopping volume distribution at the dike crest, and the derived values were compared with the two-parameter Weibull distribution [38] using the formula by [72].

The overall fair agreement of the performed comparisons demonstrated the effectiveness of the mono-static acoustic technique, characterized by the advantage of measuring flow depth and velocity synchronously in a reasonable time step. While the adopted non-intrusive instrumentations were flexible to a variety of conditions (breaking/non-breaking waves), some improvements are possible. Notably, there are limitations in the use of the acoustic profilers related to (i) the minimum seeding needed to guarantee a sufficient volume backscatter, especially in cases of high overtopping discharges; and (ii) side lobe effects, which limit velocity measurements close to the water–air interface, where higher velocities occur.

To overcome these encountered limitations, the volume scattering should be enhanced and the surface scattering limited to eventually avoid saturation and enable the detection of the Doppler effect at water gates. This could be achieved with artificial seeding to be injected under a controlled procedure in relation to the recirculating discharge (i.e., increased seeding for higher overtopping rates). Additionally, the water surface effectiveness in masking volume scattering could be reduced by limiting side lobe effects. That would be particularly relevant for the measurement of maximal velocities close to the water–air interface. This requires UVP probes in a bi-static configuration similar to the ADVP-2C by Ubertone [78]. The ultrasound emission along a vertical beam is taken apart from reception at two slant receivers, which noticeably reduces the side lobe affected thickness and provides the measurement of two components of flow velocity.

Concluding, after adjusting light exposure for videography and to artificial scattering in water and settings for acoustic probes, the integrated use of UVP and camera was demonstrated to be a reliable non-intrusive experimental apparatus to characterize dynamics induced by waves over dikes. The setup is suitable to describe wave front propagation across the crest and measure wave-by-wave overtopping discharges.

Author Contributions: Conceptualization, M.G., M.G.G. and B.Z.; methodology, M.G. and M.G.G.; formal analysis, M.G.G. and M.G.; investigation and data curation, S.M.F., G.P. and M.G.G.; writing—original draft preparation, M.G.G. and M.G.; writing—review and editing, S.M.F. and B.Z. All authors have read and agreed to the published version of the manuscript.

Funding: This research received no external funding.

Conflicts of Interest: The authors declare no conflict of interest.

Abbreviations

a	Scale parameter of the Weibull distribution (m^3)
b	Shape parameter of the Weibull distribution (-)
BS	UVP backscatter (Wm^{-2})
BS_{max}	UVP normalized maximum backscatter (-)
BS_n	UVP normalized backscatter (-)
BS_{std}	UVP normalized backscatter standard deviation (-)
$\langle BS_{std} \rangle$	Gate-averaged normalized backscatter standard deviation (-)
c	Sound speed ($m\ s^{-1}$)
d	UVP diameter (m)
EL	UVP intensity level
f	Friction coefficient (m)
f_d	Doppler shift frequency (s^{-1})
f_0	UVP signal frequency (s^{-1})
f_{prf}	UVP pulse repetition frequency (s^{-1})
g	Gravity acceleration ($m\ s^{-2}$)
G_c	Crest width of the dike (m)
h	Water depth or thickness over the dike crest (instantaneous) (m)
h_{mean}	Mean water depth or thickness over the dike crest (m)
h_{sl}	UVP side lobe affected thickness (m)
H_s	Significant wave height (m)
$L_{m-1,0}$	Spectral wave length (m)
M	Image class number (-)
x	Horizontal coordinate over the dike crest (m)
q	Mean overtopping discharge or rate ($m^3\ s^{-1}$)
P	Volume probability of not exceedance (-)
PMMA	Acronym of "Poly(methyl methacrylate"
PSD	Power spectrum density (m^2 s)
r	UVP spherical spreading or ranging distance (m)
R^2	Coefficient of determination (-)
R_c	Crest freeboard over SWL of dike (negative if the dike is submerged) (m)
$s_{m-1,0}$	Wave steepness based on spectral period (-)
SWL	Acronym of "Sea Water Level"
$T_{m-1,0}$	Spectral wave period (s)
T_p	Peak wave period (s)
T_{prf}	Pulse repetition period (s)
u	Horizontal velocity over the crest ($m\ s^{-1}$)
UVP	Acronym of "Ultrasound Doppler Velocity Profiler"
v_r	UVP radial velocity ($m\ s^{-1}$)
V	Wave-by-wave overtopping volume (m^3)
$\overline{V}$	Mean overtopping volume (m^3)
wg	Acronym of "Wave Gauges"
wd	Water depth at the wave-maker (m)
W	Image classifier matrix (-)
z	UVP maximum distance between the probe tip and the free surface (m)
α_{off}	Offshore slope of dike (°)
γ	Peak enhancement factor of Jonswap spectrum (-)
γ_b	Factor representing the influence of a berm (-)
γ_f	Factor representing the influence of the roughness (-)

γ_v	Factor representing the influence of a wave wall (-)
γ_β	Factor representing the influence of oblique waves (-)
θ	Angle between the UVP central beam and the vertical axis (°)
$\delta\theta$	Mean water surface slope (°)
$\xi_{0,m-1}$	Irribarren-Battjes breaker parameter based on spectral wave period (-)
φ	Half beam width (°)
σ	Standard deviation

References

1. Couriel, E.; Nielsen, L.; Jayewardene, I.; McPherson, B. The need for physical models in coastal engineering. *Proc. Int. Conf. Coast. Eng.* **2018**, *1*, 52. [CrossRef]
2. Lamberti, A.; Martinelli, L.; Gaeta, M.G.; Tirindelli, M.; Alderson, J. Experimental spatial correlation of wave loads on front decks. *J. Hydraul. Res.* **2011**, *49* (Suppl. 1), 81–90. [CrossRef]
3. Aleixo, R.; Soares-Frazão, S.; Zech, Y. Statistical analysis methods for transient flows–the dam-break case. *J. Hydraul. Res.* **2018**, *57*, 688–701. [CrossRef]
4. Raby, A.; Jayaratne, R.; Bredmose, H.; Bullock, G. Individual violent wave-overtopping events: Behaviour and estimation. *J. Hydraul. Res.* **2019**. [CrossRef]
5. Van Gent, M.R. Low-Exceedance Wave Overtopping Events: Measurement of Velocities and the Thickness of Water-Layers on the Crest and Inner Slope of Dikes. Delft Cluster DC030202/H3803, 2002. Delft Hydraulics. Available online: http://resolver.tudelft.nl/uuid:e71289dd-f6aa-471e-856c-832071a83753 (accessed on 1 September 2020).
6. Bosman, G.; Van der Meer, J.W.; Hoffmans, G.; Schüttrumpf, H.; Verhagen, H.J. Individual overtopping events at dikes. *Coast. Eng.* **2008**, *2009*, 2944–2956.
7. Schüttrumpf, H.F.R.; Oumeraci, H. Layer thicknesses and velocities of wave overtopping flow at seadikes. *Coast. Eng.* **2005**, *52*, 473–495. [CrossRef]
8. Van der Meer, J.W.; Hardeman, B.; Steendam, G.J.; Schüttrumpf, H.F.R.; Verheij, H. Flow depths and velocities at crest and inner slope of a dike, in theory and with the Wave Overtopping Simulator. *Coast. Eng. Proc.* **2010**, *1*, 10. [CrossRef]
9. Soares-Frazão, S.; Zech, Y.; Alcrudo, F. Laboratory Experiments, Chapter 2. In *Dam-break Problems Solutions and Case Studies*; De Wrachien, D., Mambretti, S., Eds.; WIT Press: Ashurst Lodge, UK, 2009; ISBN 978-1-84564-142-9.
10. Vousdoukas, M.I.; Kirupakaramoorthy, T.; de la Torre, M.; Wübbold, F.; Wagner, W.; Schimmels, S.; Oumeraci, H. The role of combined laser scanning and video techniques in monitoring wave-by-wave swash zone processes. *Coast. Eng.* **2014**, *83*, 150–165. [CrossRef]
11. Hofland, B.; Diamantidou, E.; van Steeg, P.; Meys, P. Wave runup and wave overtopping measurements using a laser scanner. *Coast. Eng.* **2015**, *106*, 20–29. [CrossRef]
12. Den Bieman, J.P.; de Ridder, M.P.; van Gent, M.R.A. Deep learning video analysis as measurement technique in physical models. *Coast. Eng.* **2020**, *158*, 103689. [CrossRef]
13. Kantoush, S.A.; De Cesare, G.; Boillat, J.L.; Schleiss, A.J. Flow Field Investigation in a Rectangular Shallow Reservoir using UVP, LSPIV and numerical modelling. *J. Flow Meas. Instrum.* **2008**, *19*, 139–144. [CrossRef]
14. Guerrero, M.; Latosinski, F.; Szupiany, R.N.; Nones, M.; Re, M.; Gaeta, M.G. A sediment fluxes investigation for the 2-D modelling of large river morphodynamics. *Adv. Water Resour.* **2015**, *81*, 186–198. [CrossRef]
15. Eckert, S.; Gerbeth, G.; Melnikov, V.I. Velocity measurements at high temperatures by ultrasound Doppler velocimetry using an acoustic wave guide. *Exp. Fluids* **2003**, *35*, 381–388. [CrossRef]
16. Bressan, L.; Guerrero, M.; Antonini, A.; Petruzzelli, V.; Archetti, R.; Lamberti, A.; Tinti, S. A laboratory experiment on the incipient motion of boulders by high-energy coastal flows. *Earth Surf. Process. Landf.* **2018**, *43*, 2935–2947. [CrossRef]
17. Wüthrich, D.; Pfister, M.; De Cesare, G.; Schleiss, A.J. Velocity profile measurements in bore waves. In Proceedings of the 10th International Symposium on Ultrasonic Doppler Methods for Fluid Mechanics and Fluid Engineering, Tokyo, Japan, 28–30 September 2016; pp. 137–140.

18. Wüthrich, D.; Pfister, M.; Nistor, I.; Schleiss, A.J. Experimental Study of Tsunami-Like Waves on Dry and Wet Bed Generated with a Vertical Release Technique. *J. Waterw. Port Coast. Ocean Eng.* **2018**, *144*, 04018006. [CrossRef]
19. Mariani, A.; Blacka, M.J.; Cox, R.J.; Coghkan, I.R.; Carley, J.T. Wave overtopping of coastal structures. Physical model versus desktop predictions. *J. Coast. Res.* **2009**, *SI 56*, 534–538.
20. Foote, M.; Horn, D. Video Measurement of Swash Zone Hydrodynamics. *Geomorphology* **1999**, *29*, 59–76. [CrossRef]
21. Erikson, L.H.; Hanson, H. A method to extract wave tank data using video imagery and its comparison to conventional data collection techniques. *Comput. Geosci.* **2005**, *31*, 371–384. [CrossRef]
22. Iglesias, G.; Carballo, R. Wave energy potential along the Death Coast (Spain). *Energy* **2009**, *34*, 1963–1975. [CrossRef]
23. Viriyakijja, K.; Chinnarasri, C. Wave Flume Measurement using Image Analysis. Aquat. *Procedia* **2015**, *4*, 522–531.
24. Foti, E.; Rabionet, I.C.; Marini, A.; Musumeci, R.E.; Sánchez-Arcilla, A. Experimental investigations of the bed evolution in wave flumes: Performance of 2D and 3D optical systems. *Coast. Eng.* **2011**, *58*, 606–622. [CrossRef]
25. Astruc, D.; Cazin, S.; Cid, E.; Eiff, O.; Lacaze, L.; Robin, P.; Toublanc, F.; Cáceres, I. A Stereoscopic Method for Rapid Monitoring of the Spatio-Temporal Evolution of the Sand-Bed Elevation in the Swash Zone. *Coast. Eng.* **2012**, *60*, 11–20. [CrossRef]
26. Song, J.; So, S.H.; Lim, H.C. Dynamic characteristics between waves and a floating cylindrical body connected to a tension-leg mooring cable placed in a simulated offshore environment. *Int. J. Naval Archit. Ocean Eng.* **2016**, *8*, 375–385. [CrossRef]
27. Gaeta, M.G.; Segurini, G.; Moreno, A.M.; Archetti, R. Implementation and Validation of a Potential Model for a Moored Floating Cylinder under Waves. *J. Mar. Sci. Eng.* **2020**, *8*, 131. [CrossRef]
28. Hering, F.; Leue, C.; Wierzimok, D.; Jähne, B. Particle tracking velocimetry beneath water waves. Part I: Visualization and tracking algorithms. *Exp. Fluids* **1997**, *23*, 472–482. [CrossRef]
29. Aleixo, R.; Ozeren, Y.; Altinakar, M. PIV-PTV measurements of a tailings dam-break flow. In *Hydrodynamic and Mass Transport at Freshwater Aquatic Interfaces*; Springer: Cham, Switzerland, 2016; ISBN 9783319277493.
30. Greated, C.A.; Skyner, D.J.; Bruce, T. Particle image velocimetry (PIV) in the coastal engineering laboratory. *Coast. Eng.* **1992**, *1993*, 212–225.
31. Grue, J.; Liu, P.L.F.; Pedersen, G.K. *Advances in Coastal and Ocean Engineering: PIV and Water Waves*; World Scientific Publishing Co.: Singapore, 2014; Volume 9.
32. Jayaratne, R.; Hunt-Raby, A.; Bullock, G.; Bredmose, H. Individual violent overtopping events: New insights. *Coast. Eng.* **2008**, *2009*, 2983–2995.
33. Lugni, C.; Brocchini, M.; Faltinsen, O.M. Wave impact loads: The role of the flip through. *Phys. Fluids* **2006**, *18*, 122101. [CrossRef]
34. Jensen, A. Solitary wave impact on a vertical wall. *Eur. J. Mech. B Fluids* **2019**, *73*, 69–74. [CrossRef]
35. Stansby, P.K.; Feng, T. Surf zone wave overtopping a trapezoidal structure: 1-D modelling and PIV comparison. *Coast. Eng.* **2004**, *51*, 483–500. [CrossRef]
36. Molina, R.; Ortega, M.; Moyano, J.; Losada, M. Analysis of the wave interaction with rubble-mound breakwaters using video imagery techniques. In Proceeding of Mediterranean Days of Coastal and Port Engineering, Palermo, Italy, 7–9 October 2008. PIANC.
37. Llana, A.; Molina, R.; Camarero, A.; Campos, A.; Alises, A.; López, J.D. Overtopping flow properties characterization in laboratory and prototype through the combination of non intrusive instrumental techniques. *Coast. Eng. Proc.* **2012**, *1*. [CrossRef]
38. Van der Meer, J.W.; Allsop, N.W.H.; Bruce, T.; De Rouck, J.; Kortenhaus, A.; Pullen, T.; Schüttrumpf, H.; Troch, P.; Zanuttigh, B. Manual on Wave Overtopping of Sea Defences and Related Structures. An Overtopping Manual Largely Based on European Research, But for Worldwide Application. EurOtop. 2018. Available online: www.overtopping-manual.com (accessed on 1 September 2020).
39. Galvin, C.J. Wave-height prediction for wave generators in shallow water. In *Technical Memorandum No. 4*; Army Corps of Engineers: Washington, DC, USA, 1964; pp. 1–20.
40. Wang, S. Plunger-type wavemakers: Theory and experiment. *J. Hydraul. Res.* **1974**, *12*, 357–388. [CrossRef]

41. Formentin, S.; Gaeta, M.G.; Palma, G.; Zanuttigh, B.; Guerrero, M. Flow depths and velocities across a smooth dike crest. *Water* **2019**, *11*, 2197. [CrossRef]
42. Mansard, E.P.D.; Funke, E.R. The Measurement of Incident and Reflected Spectra Using a least Squares Method. In Proceedings of the International Coastal Engineering Conference, Sydney, Australia, 23–28 March 1980.
43. Takeda, Y. Velocity profile measurement by ultrasound Doppler shift method. *Int. J. Heat Fluid Flow* **1986**, *7*, 313–318. [CrossRef]
44. Abeysekera, S.S. Performance of pulse-pair method of Doppler estimation. *IEEE Trans. Aerosp. Electron. Syst.* **1998**, *34*, 520–531. [CrossRef]
45. Muste, M.; Aberle, J.; Admiraal, D.; Ettema, R.; Garcia, M.H.; Lyn, D.; Nikora, V.; Rennie, C. *Experimental Hydraulics: Methods, Instrumentation, Data Processing and Management (IAHR Monograph)*; CRC Press: Boca Raton, FL, USA; Taylor and Francis: Oxfordshire, UK, 2017; ISBN 978-1-138-02753-4.
46. Medwin, H.; Clay, S.C. *Fundamentals of Acoustical Oceanography, Applications of Modern Acoustics*; Academic Press: Cambridge, MA, USA, 1998; ISBN 0080532160, 9780080532165.
47. Conevski, S.; Guerrero, M.; Ruther, N.; Rennie, C.D. Laboratory investigation of the apparent bedload velocity measured by ADCPs under different transport conditions. *J. Hydraul. Eng.* **2019**, *145*, 04019036. [CrossRef]
48. Urick, R.J. *Principle of Underwater Sound*, 3rd ed.; Peninsula Publishing: Los Altos Hills, CA, USA, 1983; ISBN 0-932146-62-7.
49. Longuet-Higgins, M.S. Mass Transport in Water Waves. *Philos. Trans. R. Soc. Lond. Ser. A* **1953**, *245*, 535–581.
50. Fischer, S.; Schmitt, P.; Ensminger, D.; Abda, F.; Pallares, A. A new velocity estimation method using spectral identification of noise. *Flow Meas. Instrum.* **2008**, *19*, 197–203. [CrossRef]
51. Bonmarin, P.; Rochefort, R.; Bourguel, M. Surface wave profile measurement by image analysis. *Exp. Fluids* **1989**, *7*, 17–24. [CrossRef]
52. Nguyen, H.H.; Brossard, J. Detection of wave free surface by image processing. *Eur. J. Environ. Civ. Eng.* **2008**, *12*, 307–322. [CrossRef]
53. Wang, S.; Wu, K.; Yuan, Q.; Liu, X.; Liu, Z.; Lin, X.; Zeng, R.; Zhu, H.; Dong, G.; Qian, Q.; et al. Control of grain size, shape and quality by OsSPL16 in rice. *Nat Genet* **2012**, *44*, 950–954. [CrossRef] [PubMed]
54. Canny, J. A computational approach to edge detection. *IEEE Trans. Pattern Anal. Mach. Intell.* **1986**, *8*, 679–714. [CrossRef] [PubMed]
55. Brady, P.; Boutenet, M.; Beecham, S. Free Surface Monitoring Using Image Processing. In Proceedings of the 15th Australasian Fluid Mechanics Conference, Sydney, Australia, 13–17 December 2004.
56. Ko, S.H.; Lynett, P.J. A study of long wave run-ups on a bi-linear beach slope induced by solitary and transient-focused wave group. *Coast. Eng. J.* **2019**, *61*, 135–151. [CrossRef]
57. Gaeta, M.G.; Lamberti, A. The role of air modeling on numerical investigation of coastal dynamics and wave-structure interactions. *Comput. Fluids* **2015**, *111*, 114–126. [CrossRef]
58. Guerrero, M.; Lamberti, A. Cloud Image Processing for velocity acquisition. In Proceedings of the Congress International Association for Hydraulic Research, Venice, Italy, 1–6 July 2007; Volume 1, pp. 226-1–226-11, ISBN 88-89405-06-6.
59. Maddock, I.; Harby, A.; Kemp, P.; Wood, P. *Ecohydraulics: An Integrated Approach*; John Wiley & Sons, Ltd.: Hoboken, NJ, USA, 2013; ISBN 978-0-470-97600-5.
60. Duda, R.O.; Hart, P.E.; Stork, D.G. *Pattern Classification*; John Wiley & Sons: Hoboken, NJ, USA, 2012; p. 688. ISBN 978-0-471-05669-0.
61. Van der Heijden, F.; Duin, R.P.W.; de Ridder, D.; Tax, D.M.J. *Classification, Parameter Estimation and State Estimation: An Engineering Approach Using Matlab*; Wiley: Chichester, UK, 2004; p. 440. ISBN 978-0-470-09014-5.
62. Duin, R.P.W.; Pekalska, E. *Pattern Recognition: Introduction and Terminology*; Delft University of Technology: Delft, The Netherlands, 2015; Available online: http://resolver.tudelft.nl/uuid:f5c560ed-5fc7-4320-84b4-a20614012bc7 (accessed on 1 September 2020).
63. Bouguet, J.Y. Camera Calibration Toolbox for Matlab. 2015. Available online: http://www.vision.caltech.edu/bouguetj/calib_doc/index.html (accessed on 1 September 2020).
64. Tsai, R. A versatile camera calibration technique for high-accuracy 3D machine vision metrology using off-the-shelf TV cameras and lenses. *IEEE J. Robot. Autom.* **1987**, *3*, 323–344. [CrossRef]
65. Stoica, P.; Moses, R.L. *Spectral Analysis of Signals*; Prentice Hall: Upper Saddle River, NJ, USA, 2005.

66. Zanuttigh, B.; Martinelli, L. Transmission of wave energy at permeable low-crested structures. *Coast. Eng.* **2008**, *55*, 1135–1147. [CrossRef]
67. Franco, L.; de Gerloni, M.; Van der Meer, J.W. Wave overtopping on vertical and composite breakwaters. In Proceedings of the International Coastal Engineering Conference 1994, Kobe, Japan, 23–28 October 1994.
68. Van der Meer, J.W.; Janssen, J.P.F.M. Wave runup and wave overtopping at dikes. In *Wave Forces on Inclined and Vertical Wall Structures*; Kobayashi, N., Demirbilek, Z., Eds.; ASCE: New York, NY, USA, 1995; pp. 1–27.
69. Victor, L.; Van der Meer, J.W.; Troch, P. Probability distribution of individual wave overtopping volumes for smooth impermeable steep slopes with low crest freeboards. *Coast. Eng.* **2012**, *64*, 87–101. [CrossRef]
70. Hughes, S.A.; Thornton, C.I.; van der Meer, J.W.; Scholl, B. Improvements in describing wave overtopping processes. *Proc. Int. Conf. Coast. Eng.* **2012**, *1*, 35. [CrossRef]
71. Iuppa, C.; Cavallaro, L.; Musumeci, R.E.; Vicinanza, D.; Foti, E. Empirical overtopping volume statistics at an OBREC. *Coast. Eng.* **2019**, *152*, 152. [CrossRef]
72. Zanuttigh, B.; Van der Meer, J.W.; Bruce, T.; Hughes, S. Statistical characterisation of extreme overtopping wave volumes. In *From Sea to Shore–Meeting the Challenges of the Sea: (Coasts, Marine Structures and Breakwaters 2013)*; ICE Publishing: Edinburgh, UK, 2014.
73. Pan, Y.; Lin, L.; Amini, F.; Kuang, C.; Chen, Y. New understanding on the distribution of individual wave overtopping volumes over a levee under negative freeboard. *J. Coast. Res.* **2016**, *75*, 1207–1211. [CrossRef]
74. Molines, J.; Herrera, M.P.; Gomez-Martin, M.E.; Medina, J.R. Distribution of individual wave overtopping volumes on mound breakwaters. *Coast. Eng.* **2019**, *149*, 15–27. [CrossRef]
75. Nørgaard, J.Q.H.; Lykke Andersen, T.; Burcharth, H.F. Distribution of individual wave overtopping volumes in shallow water wave conditions. *Coast. Eng.* **2014**, *83*, 15–23. [CrossRef]
76. Formentin, S.M.; Zanuttigh, B. A new fully-automatic procedure for the identification and the coupling of the overtopping waves. In Proceedings of the International Conference on Coastal Engineering 2018, Baltimore, MD, USA, 30 July–3 August 2018.
77. Gallach, D. Experimental Study of Wave Overtopping Performance of Steep Low-Crested Structures. Ph.D. Thesis, Ghent University, Ghent, Belgium, 2018; p. 182.
78. Guta, H.; Fischer, S.; Dufour, D.; Burckbuchler, M.; Fromant, G. Turbulence and sediment transport measurement with a new two components ultrasonic profiler. In Proceedings of the HydroSenSoft, International Symposium and Exhibition on Hydro-Environment Sensors and Software, Madrid, Spain, 26 February–1 March 2019.